

Final Draft
of the original manuscript:

Steglich, D.; Jeong, Y.:

**Texture-based forming limit prediction for Mg sheet alloys ZE10
and AZ31**

In: International Journal of Mechanical Sciences (2016) Elsevier

DOI: [10.1016/j.ijmecsci.2016.08.013](https://doi.org/10.1016/j.ijmecsci.2016.08.013)

Texture-based forming limit prediction for Mg sheet alloys ZE10 and AZ31

D. Steglich^a, Y. Jeong^{b,*}

^aInstitute of Materials Research, Materials Mechanics, Helmholtz-Zentrum Geesthacht, Max-Planck-Str. 1, 21502 Geesthacht, Germany

^bInternational Center for Automotive Research, Clemson University, 4 Research Drive, Greenville, SC 29607, USA

* Corresponding author: younguj@clemson.edu

ABSTRACT – A viscoplastic self-consistent crystal plasticity model was employed to study the formability of two magnesium sheet alloys, i.e., AZ31 and ZE10 at 200 °C. The flow stress-strain curves obtained by uniaxial tension tests at various strain rates and the crystallographic texture obtained from X-ray diffraction were used to calibrate the model. The crystal plasticity model was incorporated with the Marciniak-Kuczyński model in order to address the forming limits of the magnesium sheets. A good agreement of the model predictions with the experimental data obtained by Nakajima tests was achieved. The model was further studied to quantify the effects of the sample orientation with respect to laboratory axes, the amount of pre-strain applied to the sheet prior to forming, and the initial crystallographic texture. The resulting forming limit diagrams demonstrate the optimal choice of sample orientation and crystallographic texture that can lead to a significant improvement in forming limit strains.

Key Words: anisotropy, localization, VPSC, Nakajima test, Magnesium

1 Introduction

Magnesium is the lightest metal in use for the production of structural components in automotive and aircraft industries. Despite the excellent strength-to-weight ratio, the application of wrought magnesium alloys (i.e. sheets and extruded profiles) to lightweight structures is restricted due to several distinct characteristics of the materials including the pronounced mechanical anisotropy, the tension-compression asymmetry [1, 2], and their comparatively poor formability at room temperature [1, 3, 4]. These macro-mechanical characteristics are closely related to the hexagonal-close packed (HCP) crystal structure of magnesium and the presence of a strong basal texture resulting from the production process. The low crystallographic symmetry of the HCP structure leads to the intrinsically strong anisotropy on the single crystal level thus limiting easy activation of dislocation slip systems. Therefore, to assist generalized plastic flow, magnesium alloys naturally induce twinning, which subsequently leads to a significant degree of strain-induced anisotropy. Moreover, the basal texture found in wrought magnesium sheets significantly reduces the activity of basal slip upon in-plane deformation thus further limiting the accommodation of plastic deformation. Deformation in the direction of sheet thickness may be accommodated by the pyramidal slip, which is hardly active at the ambient temperature regime. The activation of this system usually requires elevated temperatures [5, 6]. Hence, recent developments to improve formability of magnesium alloys aim either on weakening the initial texture by alloying elements and changing the production process (c.f. [7]) or on assisting the activation of pyramidal slip by conducting forming operations at elevated temperatures as suggested in [8]. In order to achieve optimal formability of magnesium alloys, the interplay of crystallographic texture and the slip and twinning mechanisms should be well understood.

To the end, crystal plasticity modelling has been used to study the roles of various micro-mechanical aspects of magnesium alloys and to understand the above-mentioned macro-mechanical characteristics. Crystal plasticity models employed to full-field modelling frameworks such as the finite element method (CPFEM) and the fast-Fourier transformation (CPFFT) are proven to be useful tools for this purpose [9-13]. However, these full-field crystal plasticity models require prohibitively extensive computations so that direct employment to forming simulations is still a challenge. For this reason, the mean-field crystal plasticity method is more suitable when studying forming limits that involve numerous computational repetitions based on various boundary conditions.

The current article focuses on the formability of magnesium alloys. The formability of a sheet metal is commonly represented using forming limit diagrams (FLD) [14]. In an FLD, a forming limit curve (FLC) separates either the strain or stress space into two domains that are namely the safe and failure zones. FLCs can be experimentally determined using various methods [15-19], but the experimental procedure requires numerous sheet samples and repetitions under various strain paths causing a significant amount of experiment time. Therefore, an accurate predictive tool is highly demanded. Marciniak and Kuczyński pioneered an approach (MK approach) based on a pre-existing band to predict forming limits under multiaxial strain paths spanning from uniaxial to balanced biaxial loading conditions [20, 21]. This model has been frequently used on the basis of either macro-mechanical plasticity models [22-26] or micro-mechanical crystal plasticity frameworks [27-30]. Due to the strong anisotropy and its evolution induced by plastic deformation, macro-mechanical plasticity models with isotropic hardening are not suitable to describe the formability of magnesium alloys. Therefore in this work the micro-mechanical crystal plasticity framework based on the mean-field viscoplastic self-consistent (VPSC) model is chosen [31]. The

VPSC model has been proven to be adequate to describe various polycrystalline materials including HCP metals [12, 31-33]. To extend the VPSC model for the MK approach, the numerical algorithm recently described by Schwindt et al. [29], later extended with respect to parallel computational capabilities [34], is used in this work. Neil and Agnew [35] calculated the FLDs of similar magnesium alloys at an elevated temperature of 200 °C using a similar crystal plasticity model. However, the parameters used by Neil and Agnew were based on the room temperature behaviour, which were *extrapolated* to the elevated temperature based on various theoretical considerations. The current study takes a more straightforward method in that the material parameters were tuned by experiments conducted at 200 °C thus avoiding additional theoretical treatments.

In the current article, this model so-called VPSC-FLD is used for the following case studies to quantify the influence of three factors: 1) the insertion of initial $\{10\bar{1}2\}$ twinning to the as-received crystallographic texture following a recent study in [36], 2) the material orientation with respect to stretching axes; and 3) the initial crystallographic texture. The article is written according to the following structure. Section 2 presents the properties of two types of magnesium alloys in terms of their crystallographic texture and mechanical characteristics obtained at 200 °C. Section 3 explains the details on the material model and the calibration procedure. Section 4 presents the verification of the model in comparison with formability experiments and the aforementioned case studies. Sections 5 and 6 provide discussion on the results and the conclusion of this work, respectively.

2 Materials

2.1 **Materials under investigation**

Two different commercial magnesium rolled sheets were selected for investigation: a well-known and widely used wrought magnesium alloy AZ31 (Mg + 3%Al + 1%Zn) and an alloy with improved ductility ZE10 (Mg + 1%Zn + 0.3%Ce based mischmetal). The differences in the mechanical behaviour and the formability of the two magnesium sheet alloys have been described in earlier works, see [4, 24]. The improved ductility of ZE10 at room temperature is associated with the included rare earth elements (RE), which causes recrystallization during sheet rolling. It is hypothesized that Zn and RE additions are responsible for the modification of the rolling texture of ZE10 [3]. The two alloys are produced as sheet products in an annealed condition (O-temper) with a thickness of 1.3 mm. Both alloys have a fully recrystallized microstructure with an average grain size of 15 μm .

2.2 **Crystallographic texture**

The crystallographic texture of the as-received materials was obtained by means of X-ray diffraction [37]. The crystallographic texture was obtained from the middle sections of the sheets. Incomplete pole figures were measured up to a tilt angle of 80°. The crystallographic orientation distributions (COD) were calculated using the computer code MTEX [38]. For the subsequent modelling, the COD is represented by sampling a statistical population. The sensitivity of forming limit predictions on the number of discrete orientations is discussed in [39], where a population consisting of 2000 or more discrete orientations is recommended. In the current investigation, populations consisting of 5000 discrete orientations are considered.

The basal (0002) and prismatic ($10\bar{1}0$) pole figures drawn from the populations of discrete orientations are shown in Figure 1 where the pole figures are referenced to the material axes consisted of rolling and transverse directions that are denoted as RD and TD, respectively. In addition, the normal direction that is parallel with the thickness of the sheet is denoted as ND in what follows. The AZ31 sheet has a strong basal texture with a preferential alignment of basal planes (0002) in the sheet plane. The basal pole of the AZ31 alloy is asymmetric such that the contours in the pole figure are elongated towards the RD rather than TD suggesting that the basal pole is tilted more in the ND/RD plane than ND/TD plane. The ZE10 sheet exhibits a significantly weaker basal texture than AZ31 – the maxima in both (0002) and ($10\bar{1}0$) pole figures of ZE10 are less than those found in AZ31. Also for ZE10, note that the strongest basal pole intensity is found in the region that is slightly tilted away from the ND with several isolated contours with intensities of 1.89 and 2.47 as shown in Figure 1b. The less intense contours (≤ 0.85) in the (0002) pole of ZE10 tend to spread more in the ND/TD plane than in ND/RD.

2.3 Mechanical characterisation at 200°C

The mechanical tests described in the following were conducted in a previous study. The respective results were reported by Mekonen et al. [40]. For the sake of completeness, some results are summarized in the following.

The mechanical behaviour of the magnesium sheets at 200°C was characterized by uniaxial tension tests along three selected directions: RD, TD, and the diagonal direction (DD, i.e., the direction 45° inclined from RD). In addition, the tests in the RD were performed at three strain rates, namely 0.001/s, 0.02/s and 0.1/s. For deformation measurement, the evolution of the speckle pattern sprayed on the specimen top surface was taken as digital images and

analysed using an optical system (ARAMIS®). The axial and width strain rates (denoted as $\dot{\epsilon}_a$ and $\dot{\epsilon}_w$) were computed as functions of the load. The instantaneous r-value was calculated as below

$$r = \frac{\dot{\epsilon}_w}{-\dot{\epsilon}_a - \dot{\epsilon}_w}. \quad \text{Eq (1)}$$

Flow stress-strain curves were obtained using the logarithmic plastic strain and the true stress. Both quantities were calculated up to the maximum load, i.e. the onset of the diffuse necking.

The results of the uniaxial tension tests reveal that both AZ31 and ZE10 are anisotropic but in a different trend. The TD orientation is the strongest among the three tested in case of AZ31, while it is the weakest direction for ZE10. The evolution of the measured r-values (in Eq (1)) is also different between the two materials. In Figure 2a, a noticeable amount of anisotropy is found in AZ31 where TD gives the highest r-value and RD the lowest. On the other hand, in Figure 2b the r-values for ZE10 are not noticeably different between the three directions. Here, the DD has the highest r-value, while TD and RD reveal almost identical characteristics. In general, the degree of in-plane anisotropy, when estimated by the r-values, is higher in AZ31 than ZE10.

Nakajima-type forming limit tests using a hemispherical punch were conducted based on the ISO 12004 standard using a universal sheet metal testing machine. The testing procedure is detailed in [24]. Different from the procedure used in [24], the forming limit strains were determined according to the ISO 12004 standard by examining the strain fields recorded during each valid test. It is worth mentioning that methods to establish forming limit curves are often user and laboratory dependent. Hence, the authors are aware that the curves

presented here indicate a trend rather than image a completely deterministic process. The results of the forming limit tests are presented together with the respective model predictions in Section 4.1.

3 Material model

3.1 Visco-plastic self-consistent scheme (VPSC)

As mentioned earlier the self-consistent crystal plasticity model is used in the current article [31, 41-43]. It is briefly explained in the following.

The viscoplastic rule introduced by Asaro and Needleman [44] assumes a n-th power law relationship between the viscoplastic strain rate $\dot{\boldsymbol{\varepsilon}}$ and the local Cauchy stress tensor $\boldsymbol{\sigma}$:

$$\dot{\boldsymbol{\varepsilon}} = \dot{\gamma}_0 \sum_s \mathbf{m}^s \left(\frac{\mathbf{m}^s : \boldsymbol{\sigma}}{\tau_c^s} \right)^n \text{sgn}(\mathbf{m}^s : \boldsymbol{\sigma}), \quad \text{Eq (2)}$$

where $\dot{\gamma}_0$ is a reference strain rate; \mathbf{m}^s is the Schmid tensor of the slip systems s ; $\text{sgn}(\cdot)$ denotes the sign function being -1 or 1 depending on its argument. In Eq. (2), the rate sensitivity can be adjusted by the exponent n . The symbol τ_c^s denotes the critical resolved shear stress (CRSS) required to activate the slip (or twin) system s . An evolution of the CRSS based on a Voce hardening rule [45] is used such that

$$\tau_c^s = \tau_0^s + (\tau_1^s + \theta_1^s \Gamma) \left(1 - \exp\left(-\Gamma \left| \frac{\theta_0^s}{\tau_1^s} \right| \right) \right), \quad \text{Eq (3)}$$

in which τ_0^s and τ_1^s are the initial CRSS and the back-extrapolated increase, respectively; θ_0^s and θ_1^s are the initial and final slopes of the hardening curve, respectively; and Γ is the accumulated shear strain pertaining to the associated grain.

Rolled magnesium alloy sheets typically show a tension–compression asymmetry during in-plane deformation. This behaviour is attributed to the mechanical twinning on the $\{10\bar{1}2\}$ $\langle 10\bar{1}1 \rangle$ systems, which may be activated during c-axis tension but not during compression. Unlike slip mechanisms, twinning induces a sudden change in orientation, which is described by the Predominant Twin Reorientation Scheme (PTR) [46] in the model. For this, the shear strain ($\gamma^{t,g}$) accommodated by, twin system t of grain g is used to calculate the volume fraction of twin ($V^{t,g}$) by

$$V^{t,g} = \frac{\gamma^{t,g}}{S^t}, \quad \text{Eq (4)}$$

where S^t is the characteristic twin shear, which needs to be calibrated. The sum over all twinning systems and all grains gives the accumulated twin fraction V^{acc} in the aggregate. The grain with the highest accumulated volume fraction is allowed to rotate to the orientation defined by the twin crystallography once the accumulated volume fraction becomes larger than the threshold value

$$V^{th} = A_1 + A_2 \frac{V^{eff}}{V^{acc}}, \quad \text{Eq (5)}$$

with A_1 and A_2 being the model parameters to be calibrated and V^{eff} the (evolving) effective volume associated with the fully rotated grains. During in-plane tensile loading, the twinning

plays only a secondary role. However, the mechanism is included for the sake of completeness.

To apply the self-consistent scheme presented in [31], several linearization schemes are available. In what follows, the effective interaction scheme ($n_{\text{eff}} = 10$) is used – more details can be found, for example, in [47]. Also, for each slip (or twin) mode, a separate set of the four hardening parameters are used to characterize the strain-hardening behaviours. Additionally, self- and latent-hardening are considered using coefficients q_{ij} prescribing the ratio of the latent hardening rate of mode j to the self-hardening rate of mode i , see [48].

3.2 Incorporation of the Marciniak-Kuczyński model to VPSC

The constitutive model discussed in Section 3.1 is extended with the Marciniak-Kuczyński model [21], in which the material is assumed to consist of the homogeneous region (A) and the pre-existing groove (region B). A schematic illustration of the MK model is given in Figure 3. Three Cartesian coordinate systems are used in the following:

- 1) The laboratory Cartesian coordinate system ($\mathbf{e}_i^{\text{lab}}$ with $i=1, 2, \text{ and } 3$).
- 2) The material coordinate system ($\mathbf{e}_i^{\text{mat}}$ with $i=1,2 \text{ and } 3$); The three basis vectors align with the RD, TD and ND of the sheet, respectively. This system is inclined from the laboratory coordinate system through an in-plane rotation about the ND, which is quantified by an angular term θ .
- 3) The groove coordinate system ($\mathbf{e}_i^{\text{grv}}$) may be inclined from $\mathbf{e}_i^{\text{lab}}$ reference coordinate system by the angle ψ ; $\mathbf{e}_1^{\text{grv}}$ and $\mathbf{e}_2^{\text{grv}}$ align with \mathbf{n} and \mathbf{t} vectors, respectively. Likewise, the misorientation between $\mathbf{e}_i^{\text{grv}}$ and $\mathbf{e}_i^{\text{lab}}$ is quantified by the angle ψ .

The material coordinate system and the groove coordinate system are related to the reference laboratory Cartesian coordinates through respective transformation tensors \mathbf{R}^θ and \mathbf{R}^ψ that are functions of θ and ψ , respectively. In what follows, unless otherwise noted, tensorial properties are referenced in the laboratory coordinate system. When referenced in the other coordinate systems, a proper superscript is appended to the associated symbol.

Both regions A and B are characterized by the same constitutive description including the hardening parameters and the crystallographic texture of the as-received samples. The region B differs from region A only in terms of the initial thickness, which is quantified by f_0 such that

$$f_0 = h_0^{(B)}/h_0^{(A)} \quad \text{Eq (6)}$$

where $h_0^{(A)}$ and $h_0^{(B)}$ are the initial thicknesses of the respective regions. The initial orientation of the groove (ψ_0) that leads to the least forming limit strain for individual strain path is unknown a priori. In the current investigation, a range of ψ_0 values from 0° to 90° with an incremental angle of 5° was considered. The angle ψ_0 leading to the lowest localization strain was selected for the determination of the forming limits.

A series of monotonic deformation for the region A is parameterized by ρ , which determines the velocity gradient such that

$$\mathbf{L}_{ij}^{(A)} = c \cdot \begin{bmatrix} 1 & L_{12}^{(A)}/c & 0 \\ 0 & \rho & 0 \\ 0 & 0 & -(\rho + 1) \end{bmatrix} \mathbf{e}_i^{\text{lab}} \otimes \mathbf{e}_j^{\text{lab}}, \quad \text{Eq (7)}$$

where c is a normalizing factor introduced to keep the strain rate in the order of $10^{-3}/s$.

Note that $L_{12}^{(A)}$ is initially unknown, which has to be determined after each deformation increment. The symmetric part of $L_{ij}^{(A)}$ defines the macroscopic strain rate tensor:

$$\dot{\bar{E}}_{ij}^{(A)} = \frac{1}{2} \left(L_{ij}^{(A)} + L_{ji}^{(A)} \right). \quad \text{Eq (8)}$$

The associated macroscopic stress response pertaining to region A is:

$$\bar{\sigma}_{ij}^{(A)} = \begin{bmatrix} \bar{\sigma}_{11}^{(A)} & 0 & 0 \\ 0 & \bar{\sigma}_{22}^{(A)} & 0 \\ 0 & 0 & 0 \end{bmatrix} \mathbf{e}_i^{\text{lab}} \otimes \mathbf{e}_j^{\text{lab}}. \quad \text{Eq (9)}$$

The upper bar symbol in the respective macroscopic properties implies that the associated term should be equivalent to the weighted average of the corresponding microscopic property according to the self-consistent scheme.

The boundary condition for region B is determined as follows. Both $L_{ij}^{(A)}$ and $\bar{\sigma}_{ij}^{(A)}$ in Eqs. 10 and 11 are expressed in the groove coordinates system \mathbf{e}^{grv} through

$$L_{ij}^{(A,g)} = R_{ik}^{\psi} L_{kl}^{(A)} R_{jl}^{\psi}. \quad \text{Eq (10)}$$

and

$$\bar{\sigma}_{ij}^{(A,g)} = R_{ik}^{\psi} \bar{\sigma}_{kl}^{(A)} R_{jl}^{\psi}. \quad \text{Eq (11)}$$

Notice that the superscript g is appended to tensor components that are referenced in the groove coordinate. The compatibility conditions between regions A and B are given as

$$L_{12}^{(B,g)} = L_{12}^{(A,g)} \text{ and } L_{22}^{(B,g)} = L_{22}^{(A,g)} \quad \text{Eq (12)}$$

Note that the off-diagonal components along the thickness direction (i.e., $L_{13}^{(B,g)}$, $L_{23}^{(B,g)}$, $L_{31}^{(B,g)}$ and $L_{32}^{(B,g)}$) are prescribed as zero so that only $L_{11}^{(B,g)}$, $L_{21}^{(B,g)}$ and $L_{33}^{(B,g)}$ remain unknown. The force equilibrium can be expressed in the \mathbf{e}^{grv} coordinate system such that

$$\bar{\sigma}_{11}^{(B,g)} = \frac{1}{f} \bar{\sigma}_{11}^{(A,g)} \text{ and } \bar{\sigma}_{12}^{(B,g)} = \frac{1}{f} \bar{\sigma}_{12}^{(A,g)} \quad \text{Eq (13)}$$

where f is the current value of inhomogeneity factor that evolves from f_0 through:

$$f = f_0 \exp(E_{33}^{(B)} - E_{33}^{(A)}). \quad \text{Eq (14)}$$

Likewise, the shear components along the thickness direction (i.e., $\bar{\sigma}_{13}^{(B,g)}$ and $\bar{\sigma}_{23}^{(B,g)}$) and $\bar{\sigma}_{33}^{(B,g)}$ component are zero thus leaving only $\bar{\sigma}_{22}^{(B,g)}$ unknown. Eqs. 12 and 13 provide the boundary condition for region B so that the unknown components (i.e., $\bar{\sigma}_{22}^{(B,g)}$, $L_{11}^{(B,g)}$, $L_{21}^{(B,g)}$, and $L_{33}^{(B,g)}$) will be determined as the results of self-consistent calculation at each deformation increment. After each successful incremental step, the orientation of the groove (i.e. the co-rotating coordinate system \mathbf{e}^{grv}) is updated following the procedure described in [49]:

Eq (15)

$$\begin{pmatrix} n_1 \\ n_2 \end{pmatrix} = \frac{1}{\sqrt{t_1^2 + t_2^2}} \begin{pmatrix} t_2 \\ -t_1 \end{pmatrix}$$

$$\text{with } t_1 = F_{11}t_1^0 + F_{12}t_2^0 \text{ and } t_2 = F_{21}t_1^0 + F_{22}t_2^0,$$

where \mathbf{F} is the deformation gradient tensor; \mathbf{t}^0 is the initial direction of the tangent vector \mathbf{t} .

The localization criterion is given as:

Eq (16)

$$\left| L_{33}^{(B)} \right| \geq 10 \left| L_{33}^{(A)} \right|.$$

In order to obtain a forming limit curve, various strain paths should be probed for region A. Moreover, for each strain path, a number of region B simulations should be performed in order to find the initial groove angle ψ_0 that leads to the minimum localization strain. In this study, 8 separate strain paths were probed for region A at a fixed value of θ . Since 19 separate ψ_0 angles (from 0° to 90° with an incremental angle of 5°) are considered, in total 152 separate simulations are required for region B. Additionally, various θ angles are examined from 0° to 90° with an increment of 15° to study the influence of anisotropy when the stretching axes are inclined from the given material axes. It is important to note that the region B simulations are independent from one set of (ρ, ψ_0, θ) to another. In the VPSC-FLD code, those independent simulations are allowed to run in parallel by utilizing Python's multiprocessing package [34, 39, 50].

3.3 VPSC Parameter Calibration

For the prediction of the forming limits using the crystal plasticity model described above, several model parameters need to be calibrated. To that end, the hardening parameters (i.e.,

τ_0, τ_1, θ_0 and θ_1 for each deformation mode) were determined using the Levenberg-Marquardt minimisation algorithm together with VPSC simulations of the mechanical tests described in Section 2.3. A set of initial parameters was chosen and simulations of the mechanical tests were conducted with these parameters. The difference between the simulations and the measurements was evaluated and a new set of parameters was calculated. This process was repeated until the difference was reduced to a sufficiently small value. The experimental input for this iterative procedure consists of the uniaxial tension stress-strain curves and the evolution of the r-value as a function of the longitudinal strain measured along the RD, TD, and DD. Figure 2 shows the result of the calibration process in comparison to the experimental data at an initial strain rate of 0.01 /s. Whereas the agreement in the case of AZ31 can be regarded as excellent, such the fit for ZE10 was not as good. In this particular case, special focus was placed on the r-value agreement, as this is expected to have a significant influence on the localization behaviour [34]. In the second (iterative) step, the rate sensitivity exponent n (see Eq. 2) was determined. While the reference slip/twinning rate $\dot{\gamma}_0$ was assumed to be 0.001 /s regardless of the slip/twin system, the rate sensitivity exponent was determined from the tension tests along the RD with three different initial strain rates, namely 0.001 /s, 0.02 /s, and 0.1 /s. The results of fitting are depicted in Figure 4 and the types of deformation mechanisms and the calibrated parameters are listed in Tables 1 and 2, respectively.

Despite its low activity, the twinning mechanism was included in the modelling. The respective hardening parameters were calibrated from the tensile tests. However, a proper estimate for the parameters related to the grain reorientation is best done based on in-plane compression data, which were not available in the current investigation. Consequently, the parameters S^t, A_1 and A_2 were set to obtain the typical sigmoidal stress-strain response of

magnesium alloys in during compression. For both alloys, 0.25, 0.25 and 0.98 were used, respectively.

4 Results

4.1 Verification of the model

In Figure 5, the experimental FLCs are compared with the corresponding model predictions. Note that the FLCs are plotted in the principal strain space (\bar{E}_1, \bar{E}_2) . In the case of AZ31 shown in Figure 5a, the initial inhomogeneity factor f_0 of 0.995 was used. This value was iteratively determined to achieve a global agreement with the test results. With the monotonic linear strain paths, the slope of the predicted FLC in $\rho < 0$ (the left part of the FLD) is slightly lower than what was experimentally obtained. Under the monotonic linear strain paths, the minimum forming limit strain is predicted in the plane strain path (i.e., $\rho = 0$). On the other hand, the experimental data obtained by the Nakajima method show that the minimum formability is obtained in a strain path that is slightly deviated from plane strain towards the biaxial path (i.e., $\rho \approx 0.1$). In the case of ZE10, Figure 5b shows that the predictions under the monotonic linear strain paths are in good agreement with the experimental forming limit strains, where the initial inhomogeneity f_0 of 0.999 was used.

It is important to note that in the Nakajima tests the specimens initially experience nearly balanced biaxial stretching since the initial bending is induced by the contact with the hemispherical punch (see e.g. [24] for the strain paths measured on the top surface). In order to approximately account for this stretching, a pre-strain of $(\bar{E}_{11}, \bar{E}_{22}) = (0.025, 0.025)$ was prescribed in the simulations prior to the monotonic linear strain paths. Note that during this pre-strain, both strain hardening and texture evolution were accounted for and the

subsequent calculations were conducted based on the *evolved* polycrystalline aggregates. In the case of AZ31, the consideration of the pre-strain led to better agreement with the experimental data in comparison with the predictions resulting from the monotonic linear strain paths in that the slope of the FLC increased in the region $\rho < 0$, and the forming limit strains near $\rho = 0$ reduced, see Figure 5a. Also, note that the pre-strain shifted the location of the minimum forming limit strain towards the balanced biaxial path ($\rho > 0$), which is consistent with the experimental observation. In contrast, the pre-strain had a negligible influence for ZE10 in the region $\rho < 0$ while slightly reduced the forming limit strains for $0 < \rho \leq 0.5$, see Figure 5b.

The boundary condition presented in Eqs 7 and 9 assumes that $\bar{\sigma}_{12}^A = 0$ while $\bar{L}_{12}^A \neq 0$. Note that the boundary condition of $\bar{\sigma}_{12}^A \neq 0$ and $\bar{L}_{12}^A = 0$ is also plausible. The two boundary conditions may result in different results as described in [29, 49]. In fact, both boundary conditions are two extreme assumptions and the true boundary condition may potentially reside between these two types. Nevertheless, the fact that DIC map shows a non-zero shear strain (not shown in the paper) and the use of the current boundary condition leads to reasonable agreement with the experimental forming limit diagram supports the current boundary.

4.2 Effect of sheet orientation

The FLCs were calculated for different orientations of the sheet with respect to the laboratory axes, to which the experimental strain paths are referenced. This was realized by investigating various θ values: $\theta = 0^\circ$ to 90° with an increment of 15° . As shown in Figures 6 and 7 for AZ31 and ZE10, respectively, the FLC predictions were significantly altered by this rotation. Note that for each of the simulated polycrystals, FLCs in Figures 6 and 7 were

plotted in two separate strain spaces: one in $(\bar{E}_{11}, \bar{E}_{22})$ and another in the principal strain space (\bar{E}_1, \bar{E}_2) . In the case of AZ31 (Figure 6), the orientations of $\theta = 30^\circ$ and 45° led to the best forming capacity among the tested strain paths both in $(\bar{E}_{11}, \bar{E}_{22})$ and (\bar{E}_1, \bar{E}_2) spaces. On the other hand, in Figure 7 ZE10 shows a path-dependent tendency in that $\theta = 0^\circ$ and 15° led to equally superior forming limit strains towards uniaxial for $\rho < -0.25$ in both strain spaces while $\theta = 90^\circ$ is the most favourable choice for $\rho > 0$. The increased forming capacity for ZE10 is more pronounced in the $(\bar{E}_{11}, \bar{E}_{22})$ space than in the principal strain space.

4.3 Effect of initial $\{10\bar{1}2\}$ twin

In order to improve the stretch formability of rolled magnesium alloys, it is suggested to induce $\{10\bar{1}2\}$ twins prior to forming [36, 51]. In the current investigation, this was achieved by using the crystallographic texture obtained after in-plane compressive deformation. To that end, an intermediate texture was calculated from a separate VPSC simulation for compression along the TD orientation with a strain of 0.04. The reorientation of grains calculated on the basis of the PTR-scheme described in Section 3.1 led to a change of the initial texture. For both alloys, a significant portion of grains reoriented due to this compressive loading, which led to the emergence of strong (0002) pole intensities in the TD, as shown in Figure 8. Figure 9 shows the FLCs of both AZ31 and ZE10 based on these intermediate textures. Each of the FLCs shown in Figure 9 is the combined result of two separate θ angles: $\theta = 0^\circ$ that is $\mathbf{e}_1^{\text{lab}} \parallel \text{RD}$; and $\theta = 90^\circ$ that is $\mathbf{e}_1^{\text{lab}} \parallel \text{TD}$. Depending on the θ angle, distinct changes in the FLCs were found in Figure 9. In the case of $\theta = 0^\circ$, the addition of $\{10\bar{1}2\}$ twin led to a systematic expansion of the safe-zone in the FLD for both AZ31 and ZE10. In the case of $\theta = 90^\circ$, while ZE10 shows a systematic increase in forming

limit strains except for $0.8 \leq \rho \leq 1$, the results of AZ31 are more significantly path-dependent, that is, a slight reduction for $0 \leq \rho \leq 0.6$ and increase for $\rho < 0$.

4.4 Model textures

To investigate the influence of various crystallographic textures on the forming limits, the following model textures are considered:

1) A uniform random texture (isotropic) mimicking a cast alloy. This model texture is considered for both AZ31 and ZE10 polycrystals.

2) For AZ31 polycrystal, the strong basal pole is split into less intense ones that are tilted away from the ND towards the RD. Those textures were evidenced after rolling and annealing of rare earth containing magnesium alloys, see [52]. Two separate tilt angles are considered: 30° and 50° as shown in Figures 10a and 10b. These textures are named bipole30 and bipole50, respectively.

3) In the case of ZE10, the basal pole is symmetrically tilted away from the ND that is similar with the experimental observation discussed in Section 2.2. In order to investigate the influence of such tilting, two idealized textures are considered with distinct tilting angles: 30° and 50° . This leads to doughnut-shaped basal textures, as shown in Figures 11a and 11b, named doughnut30 and doughnut50, respectively.

Figures 12 and 13 show the FLCs predicted using the model textures of AZ31 (Figure 10) and ZE10 (Figure 11), respectively. Note that the FLCs shown in Figures 12 and 13 follow the same mapping convention as in Figure 9: the two separate results from $\theta = 0^\circ$ and 90° are combined to a single FLC plotted in the $(\bar{E}_{11}, \bar{E}_{22})$ strain space. For the model textures under the current consideration, the FLDs plotted in $(\bar{E}_{11}, \bar{E}_{22})$ space should not be

significantly deviated from those in the principal strain space due to the orthogonal symmetry commonly found in the current model textures. Figure 12 includes the FLC predictions for the random, bipole30 and bipole50 textures in comparison with the prediction based on the experimental texture of the as-received AZ31, see Figure 1. For $\rho < 0.2$ with $\theta = 90^\circ$ (i.e., $\mathbf{e}_1^{\text{lab}} \parallel \text{TD}$) towards the uniaxial strain path along the TD, the bipole30 and bipole50 led to significantly improved formability compared to the measured texture, whereas the changes for $0.2 < \rho < 1$ are not that pronounced. In the case of $\theta = 0^\circ$ (i.e., $\mathbf{e}_1^{\text{lab}} \parallel \text{RD}$), the gain of formability is more noticeable and systematic regardless of the strain path. The FLC prediction based on the random isotropic texture also led to systematic expansion of the safe-domain in the FLD. Its improvement in $\theta = 90^\circ$ is superior to the other textures. On the other hand, in $\theta = 0^\circ$ the improvement by the random texture is less pronounced in comparison with that obtained by bipole50. Nevertheless, the improvement in the equi-biaxial strain path (i.e., $\rho = 1$) is superior to the other cases. Also, notice that the random isotropic texture led to the FLC that has mirror-symmetry with respect to the equi-biaxial strain path.

Figure 13 shows the FLCs pertaining to ZE10. Both doughnut30 and doughnut50 textures are axi-symmetric about the ND, thus the resulting FLCs are mirror-symmetric with respect to the equi-biaxial strain path. The doughnut50 texture resulted in a systematically expanded safe zone in the FLD compared with the result based on the experimental texture, whereas the doughnut30 led to a systematic reduction of the safe zone. The random isotropic texture also provided a systematic expansion of the safe zone in the FLD in comparison with the result based on the experimental texture. Nevertheless, the improvement is less pronounced in comparison with the doughnut30.

5 Discussion

Various material parameters required for the current VPSC model, including the slip/twinning hardening parameters, the latent hardening matrix, and the strain rate sensitivity, were calibrated using the empirical fitting procedure discussed in Section 3.3. The model was capable of successfully describing the two magnesium sheets in terms of the anisotropy in flow stress curve, the r-value evolution three loading directions (Figure 2), and the strain rate sensitivity (Figure 4). However, it is more preferable to determine the parameters based on the underlying physical mechanisms. Such an attempt has been reported in [53], where the interactions between the slip systems of a pure magnesium alloy were quantified by discrete dislocation dynamics simulations. As the transferability of the complete latent hardening matrix from pure magnesium to WE43 was shown [54], this method can be potentially useful for other magnesium alloys as well. To that end, during a preliminary investigation of the current work, the latent hardening parameters obtained in [53] was examined. However, this method did not lead to any improvement in terms of the r-value prediction. This might be related to difference in the temperature regime, the unknown temperature dependency in the slip interactions; and the presence of precipitates in the materials under investigation.

Regarding the predictions shown in Figure 5, the path change approximated by the initial balanced biaxial strain led to a shift in FLC, which is consistent not only with the current experimental data shown in Figure 5a but also with the general trends found in other studies see [55-57]. The AZ31 sample was particularly sensitive to the pre-biaxial strain. Therefore, at least for AZ31, the forming limit data should be obtained using planar forming limit

experiments with a flat punch, which can avoid bending that is inevitable with a hemispherical punch [18].

Among the three case studies with the calibrated model, the first study was to quantify the effect of the misorientation between the material axes and the stretching axes. Similar studies are found in the literature but often confined to a limited number of cases, for instance, only for 0°, 45° and 90° angles in [58] using a similar model. The self-consistent crystal plasticity framework is computationally more intensive than Taylor crystal plasticity model [59] so that a parametric study with a vast array of factors may require a large amount of computation time. In the current study, a set of seven θ angles was tested using the VPSC-FLD model thanks to the improvement in computational efficiency by employing the parallel computation using Python's multiprocessing package [34] and the advanced algorithm in [29]. The results shown in Figures 6 and 7 imply that an optimal direction of stretching can be predicted using this model. The ISO standard for forming limit experiments [60] recommends that the orientation of sheet with respect to the laboratory axes should be the one that gives minimum values of forming limit strains. However, experimental determination of the correct θ can be very costly. More importantly, according to the VPSC-FLD calculation for the current magnesium alloys, there might not be a universal direction of stretching that guarantees the lowest limit strains regardless of the strain path. Note that the optimal value of θ for a given strain path varies as evidenced in the predictions for ZE10 (see Figure 7). Also, the resulting FLCs are sensitive to the choice of strain space. The ISO standard method [60] defines the FLC in the principal strain space, which presumably originates from the use of circular grids, with which it is difficult to measure strain in the a global coordinate system. As the digital image correlation technique is now widely spread, such a restriction seems unnecessary.

The second case study was to verify if the initial activation of $\{10\bar{1}2\}$ twin leads to improvement in forming limits as suggested in [36, 51] using the current VPSC-FLD model. The pre-compression along the TD successfully induced the twinning and the subsequent changes in the texture as shown in Figure 8. Overall, the safe domain in the FLD was expanded for both magnesium alloys (Figure 9). This result supports the idea suggested in [36, 51], where the formability enhancement by initial twinning was tested only at a particular set of strain paths (close to biaxial tension using limit dome height test). However, the gain in formability predicted by the model is not pronounced. The path-sensitive improvement demonstrated by VPSC-FLD (Figure 9) suggests that more thorough experimental tests that cover the complete strain path are necessary.

The third case study using modifications in the as-received textures shown in Figures 10 and 11 led to more significant changes in FLC. Commonly in Figures 12 and 13, it was shown that the random isotropic texture led to a noticeable improvement in comparison with the result based on the as-received texture. However, the isotropic texture did not lead to a universal enhancement in formability. Instead, for AZ31 the tailored textures (i.e., Bipole30 and Bipole50) outperformed the isotropic texture depending on the strain paths. For ZE10, Doughnut50 texture led to a global improvement regardless of the strain path. On the contrary, Doughnut30 led to a significant reduction of the safe-domain in FLD. Overall, the results suggest that 1) increasing the angular distance between the two separated basal poles would improve the forming limit curves; 2) tailored textures specific for each magnesium alloy may lead to more significant improvement in formability than the isotropic random texture.

6 Conclusions

AZ31 and ZE10 magnesium alloys were studied by the VPSC-FLD model. The material parameters were tuned by uniaxial tension tests conducted at 200 °C along various directions and additional tests with various strain rates in order to account for strain-rate sensitivity. The model well captures the anisotropy in terms of flow stress and r-value evolution for the two magnesium alloys.

The model was further investigated by comparing with the forming limit data obtained by Nakajima testing at 200 °C. By accounting for the initial balanced biaxial strain induced by the hemispherical punch a good agreement was found between the predicted and experimental FLCs for both magnesium alloys. As a follow-up to this validation procedure, the model was used to conduct three case studies:

- 1) Various angles between the principal stretching axes and the material axes were tested. It was confirmed that the optimal angle leading to an increase in forming limit strain depends on the strain path.
- 2) The second study was conducted to verify the effect of preceding $\{10\bar{1}2\}$ twinning. The result supports that the addition of $\{10\bar{1}2\}$ twins weakens the texture thus leading to an extension of safe-domain in the FLD for both alloys.
- 3) In the third study, an isotropic texture (random texture) and various idealized initial textures were selected to quantify their respective effect on the FLCs. The VPSC-FLD model predicted an improvement of formability by the isotropic texture regardless of strain path. The forming limit strain increased compared to the as-received texture. However, the use of tailored crystallographic textures led to a more significant improvement. Hence,

texture design appears to be well suited in order to improve the formability of wrought products.

The model appears useful to reduce or circumvent expensive testing effort for determining conventional forming limits. It assists the selection of the optimal stretching direction for the given anisotropy and it allows suggesting optimal textures to the microstructural design community.

7 Acknowledgments

The authors thank Ricardo Lebensohn and Carlos Tomé for providing a version of VPSC program (7c). The fruitful discussions with Sean Agnew, Sangbong Yi and Mark Iadicola are appreciated. The authors also kindly acknowledge the careful review by Jeongyeon Lee.

LITERATURE

1. Hosford, W.F., *The mechanics of crystals and textured polycrystals*. 1993, New York: Oxford University Press.
2. Hosford, W.F. and T.J. Allen, *Twinning and directional slip as a cause for a strength differential effect*. Metallurgical Transactions, 1973. **4**(5): p. 1424-1425.
3. Bohlen, J., et al., *The texture and anisotropy of magnesium–zinc–rare earth alloy sheets*. Acta Mater., 2007. **55**: p. 2101-2112.
4. Yi, S., et al., *Mechanical anisotropy and deep drawing behaviour of AZ31 and ZE10 magnesium alloy sheets*. Acta Materialia, 2009. **58**(2): p. 592-605.
5. Yoo, M.H., et al., *Nonbasal deformation modes of HCP metals and alloys: role of dislocation source and mobility*. Metall. Mater. Trans. A, 2002. **33A**: p. 813-822.
6. Wonsiewicz, B. and W. Backofen, *Independent slip systems and ductility of hexagonal polycrystals*. Transaction of Metallurgical Soc. AIME, 1967. **239**: p. 1422-1433.
7. Kainer, K.U., et al., *Development of the Microstructure and Texture of RE containing Magnesium Alloys during Hot Rolling*. Materials Science Forum, 2010. **654-656**: p. 580-585.
8. Ion, S.E., F.J. Humphreys, and S.H. White, *Dynamic recrystallisation and the development of microstructure during the high temperature deformation of magnesium*. Acta Metallurgica, 1982. **30**(10): p. 1909-1919.
9. Segurado, J., et al., *Multiscale modeling of plasticity based on embedding the viscoplastic self-consistent formulation in implicit finite elements*. International Journal of Plasticity, 2012. **28**(1): p. 124-140.
10. Lebensohn, R., *N-site modeling of a 3D viscoplastic polycrystal using fast Fourier transform*. Acta Materialia, 2001. **49**(14): p. 2723-2737.
11. Graff, S., W. Brocks, and D. Steglich, *Yielding of magnesium: From single crystal to polycrystalline aggregates*. Int. J. Plast., 2007. **23**(12): p. 1957-1978.
12. *Mechanism of Twinning in Metals*, in *Nature*. 1929. p. 262-263.
13. Guillemer, C., M. Clavel, and G. Cailletaud, *Cyclic behavior of extruded magnesium: Experimental, microstructural and numerical approach*. International Journal of Plasticity, 2011. **27**(12): p. 2068-2084.
14. Keeler, S.P. and W.A. Backofen, *Plastic Instability and Fracture in Sheet Stretched over Rigid Punches*. Trans. of the A. S. M., 1963. **56**(1): p. 25-48.
15. Hasek, V.V., *Untersuchung und theoretische Beschreibung wichtiger Einflußgrößen auf das Grenzformänderungsschaubild. Teil 1*. Blech Rohre Profile, 1978. **25**: p. 213- 220.
16. Hasek, V.V., *Untersuchung und theoretische Beschreibung wichtiger Einflußgrößen auf das Grenzformänderungsschaubild. Teil 2*. Blech Rohre Profile, 1978. **25**: p. 285- 292.
17. Hasek, V.V., *Untersuchung und theoretische Beschreibung wichtiger Einflußgrößen auf das Grenzformänderungsschaubild. Teil 3*. Blech Rohre Profile, 1978. **25**: p. 493- 499.
18. Raghavan, K.S., *A simple technique to generate in-plane forming limit curves and selected applications*. Metallurgical and Materials Transactions A, 1995. **26**(8): p. 2075-2084.
19. Nakazima, K., T. Kikuma, and K. Hasuka, *Study on the formability of steel sheets*, F.R. Laboratory, Editor. 1971. p. 141-154.
20. Marciniak, Z. and K. Kuczynski, *Limit strains in the processes of stretch-forming sheet metal*. International Journal of Mechanical Sciences, 1967. **9**(9): p. 609-620.

21. Marciniak, Z., K. Kuczynski, and T. Pokora, *Influence of the plastic properties of a material on the forming limit diagram for sheet metal in tension*. International Journal of Mechanical Sciences, 1973. **15**(10): p. 789-800.
22. Cao, J., et al., *Prediction of localized thinning in sheet metal using a general anisotropic yield criterion*. International Journal of Plasticity, 2000. **16**(9): p. 1105-1129.
23. Butuc, M.C., et al., *A more general model for forming limit diagrams prediction*. Journal of Materials Processing Technology, 2002. **125-126**: p. 213-218.
24. Mekonen, M.N., et al., *Experimental and numerical investigation of Mg alloy sheet formability*. Materials Science and Engineering: A, 2013. **586**: p. 204-214.
25. Stoughton, T.B. and J.W. Yoon, *Anisotropic hardening and non-associated flow in proportional loading of sheet metals*. International Journal of Plasticity, 2009. **25**(9): p. 1777-1817.
26. Stoughton, T.B., *A general forming limit criterion for sheet metal forming*. International Journal of Mechanical Sciences, 2000. **42**(1): p. 1-27.
27. Wu, P.D., et al., *Crystal plasticity forming limit diagram analysis of rolled aluminum sheets*. Metallurgical and Materials Transactions A, 1998. **29**(2): p. 527-535.
28. Wang, H., et al., *On crystal plasticity formability analysis for magnesium alloy sheets*. International Journal of Solids and Structures, 2011. **48**(6): p. 1000 - 1010.
29. Schwindt, C., et al., *Experimental and Visco-Plastic Self-Consistent evaluation of forming limit diagrams for anisotropic sheet metals: An efficient and robust implementation of the M-K model*. International Journal of Plasticity, 2015(0).
30. Signorelli, J. and M. Bertinetti, *On the role of constitutive model in the forming limit of FCC sheet metal with cube orientations*. International Journal of Mechanical Sciences, 2009. **51**(6): p. 473-480.
31. Lebensohn, R.A. and C.N. Tomé, *A self-consistent anisotropic approach for the simulation of plastic deformation and texture development of polycrystals: Application to zirconium alloys*. Acta Metallurgica Et Materialia, 1993. **41**(9): p. 2611-2624.
32. Ebeling, T., et al., *Material law parameter determination of magnesium alloys*. Materials Science and Engineering: A, 2009. **527**(1-2): p. 272-280.
33. Steglich, D., et al., *Biaxial deformation behaviour of AZ31 magnesium alloy: Crystal-plasticity-based prediction and experimental validation*. International Journal of Solids and Structures, 2012. **49**(25): p. 3551-3561.
34. Jeong, Y., et al., *Forming limit prediction using a self-consistent crystal plasticity framework: a case study for body-centered cubic materials*. Modelling and Simulation in Materials Science and Engineering, 2016. **24**: p. 055005.
35. Neil, J.C. and S.R. Agnew, *Crystal plasticity-based forming limit prediction for non-cubic metals: Application to Mg alloy AZ31B*. International Journal of Plasticity, 2009. **25**: p. 379-398.
36. Park, S.H., S.-G. Hong, and C.S. Lee, *Enhanced stretch formability of rolled Mg-3Al-1Zn alloy at room temperature by initial {10-12} twins*. Materials Science and Engineering: A, 2013. **578**: p. 271-276.
37. Mekonen, M.N., *Experimental and Numerical Investigation of Mg Alloy Sheet Forming*. 2011, Christian-Albrecht Universität zu Kiel: Kiel.
38. Bachmann, F., R. Hielscher, and H. Schaeben, *Texture Analysis with MTEX – Free and Open Source Software Toolbox*. Solid State Phenomena, 2010. **160** p. 63-68.
39. Jeong, Y., et al., *Forming limit diagram predictions using a self-consistent crystal plasticity model: a parametric study*. Key Engineering Materials, 2015. **651**: p. 193-198.

40. Mekonon, M.N., et al., *Mechanical characterization and constitutive modeling of Mg alloy sheets*. Materials Science and Engineering: A, 2012. **540**: p. 174-186.
41. Hill, R., *A self-consistent mechanics of composite materials*. Journal of the Mechanics and Physics of Solids, 1965. **13**(4): p. 213 - 222.
42. Molinari, A., G.R. Canova, and S. Ahzi, *A self consistent approach of the large deformation polycrystal viscoplasticity*. Acta Metallurgica, 1987. **35**(12): p. 2983 - 2994.
43. Hutchinson, J.W., *Bounds and self-consistent estimates for creep of polycrystalline materials*. Proc. R. Soc. A, 1976. **348**: p. 101-127.
44. Asaro, R.J. and A. Needleman, *Texture development and strain hardening in rate dependent polycrystals*. Acta Metall., 1985. **33**(6): p. 923-953.
45. Voce, E., *The relationship between stress and strain for homogeneous deformation*. J. Inst. Metals, 1948. **74**: p. 537-562.
46. Tomé, C.N., R.A. Lebensohn, and U.F. Kocks, *A model for texture development dominated by deformation twinning: Application to zirconium alloys*. Acta Metallurgica et Materialia, 1991. **39**(11): p. 2667-2680.
47. Tomé, C., *Self-consistent polycrystal models: a directional compliance criterion to describe grain interactions*. Modelling and Simulation in Materials Science and Engineering, 1999. **7**(5): p. 723.
48. Wang, H., et al., *Numerical Analysis of Large Strain Simple Shear and Fixed-End Torsion of HCP Polycrystals*. Computers Materials and Continua, 2010. **19**(3): p. 255-284.
49. Kuroda, M. and V. Tvergaard, *Forming limit diagrams for anisotropic metal sheets with different yield criteria*. International journal of solids and structures, 2000. **37**(37): p. 5037-5059.
50. Jones, E., et al. *SciPy: Open source scientific tools for Python*. 2001.
51. Song, B., et al., *Improvement of formability and mechanical properties of magnesium alloys via pre-twinning: A review*. Materials & Design, 2014. **62**: p. 352-360.
52. Hirsch, J. and T. Al-Samman, *Superior light metals by texture engineering: Optimized aluminum and magnesium alloys for automotive applications*. Acta Materialia, 2013. **61**(3): p. 818-843.
53. Bertin, N., et al., *On the strength of dislocation interactions and their effect on latent hardening in pure Magnesium*. International Journal of Plasticity, 2014. **62**: p. 72-92.
54. Bhattacharyya, J.J., et al., *Demonstration of alloying, thermal activation, and latent hardening effects on quasi-static and dynamic polycrystal plasticity of Mg alloy, WE43-T5, plate*. International Journal of Plasticity.
55. Laukonis, J.V. and A.K. Ghosh, *Effects of strain path changes on the formability of sheet metals*. Metallurgical Transactions A. **9**(12): p. 1849-1856.
56. Barata da Rocha, A., F. Barlat, and J.M. Jalinier, *Prediction of the forming limit diagrams of anisotropic sheets in linear and non-linear loading*. Materials Science and Engineering, 1985. **68**(2): p. 151-164.
57. Graf, A. and W. Hosford, *The influence of strain-path changes on forming limit diagrams of Al 6111 T4*. International Journal of Mechanical Sciences, 1994. **36**(10): p. 897-910.
58. Signorelli, J.W., M.J. Serenelli, and M.A. Bertinetti, *Experimental and numerical study of the role of crystallographic texture on the formability of an electro-galvanized steel sheet*. Journal of Materials Processing Technology, 2012. **212**(6): p. 1367-1376.
59. Taylor, G.I., *Plastic strain in metals*. J. of Inst. Metals, 1938. **62**.

60. ISO, *Metallic materials -- Sheet and strip -- Determination of forming-limit curves, in Part 2: Determination of forming-limit curves in the laboratory.*

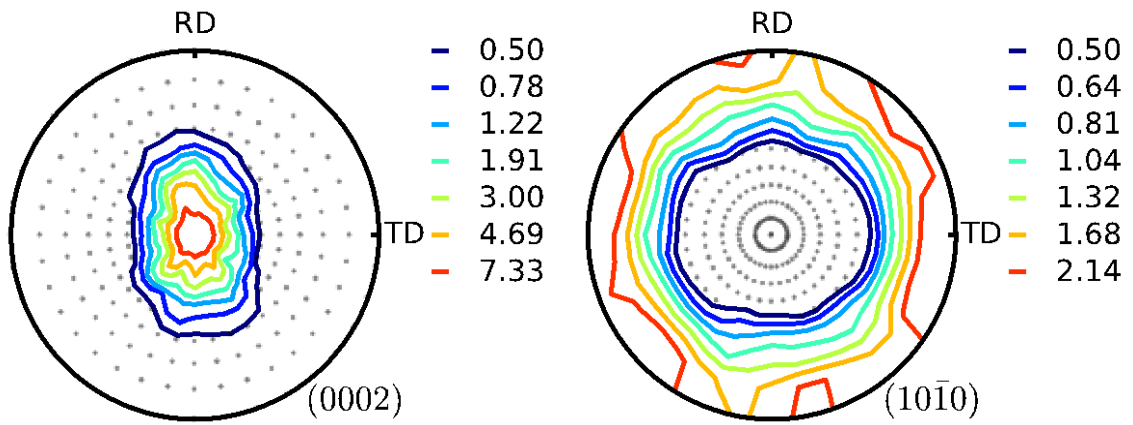
Table 1: Deformation modes considered in the present work

i	Name	Plane	Slip/twin direction
1	Basal slip	(0001)	$\langle 2\bar{1}\bar{1}0 \rangle$
2	Prismatic slip	(10 $\bar{1}$ 0)	$\langle \bar{1}2\bar{1}0 \rangle$
3	Pyramidal slip	(10 $\bar{1}$ 1)	$\langle \bar{1}\bar{1}23 \rangle$
4	Tensile twin	(10 $\bar{1}$ 2)	$\langle \bar{1}011 \rangle$

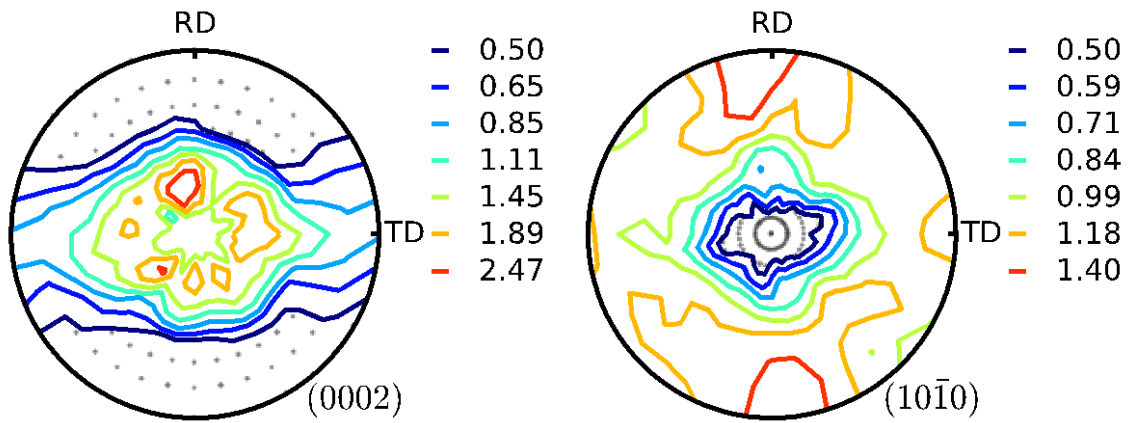
Table 2: Parameters pertaining to each deformation mode in Table 1 for AZ31 and ZE10, respectively; Hardening parameters (i.e., τ^0 , τ^1 , θ_0 , and θ_1) are in [MPa] unit, while the rate-sensitivity (n) and latent hardening ratio (q_{i4}) are dimensionless.

Material	n	Parameter	Basal	Prismatic	Pyramidal	Tensile Twinning
AZ31	12.0	τ^0	22	56	58	29
		τ^1	15	28	53	0
		θ_0	200	367	710	0
		θ_1	2	0	0	0
		q_{i4}	4.0	1.2	1.2	1.0
ZE10	22.0	τ^0	25	49	100	31
		τ^1	34	0	10	0
		θ_0	166	207	200	0
		θ_1	0	10	1	0
		q_{i4}	1.2	1.2	1.2	1.0

Figures

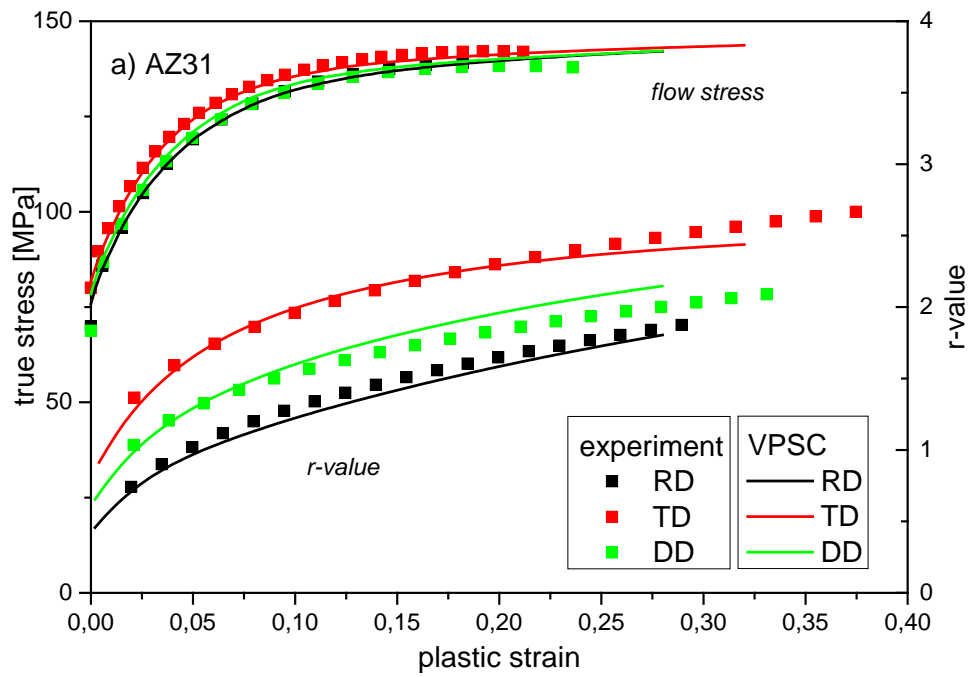


(a) AZ31

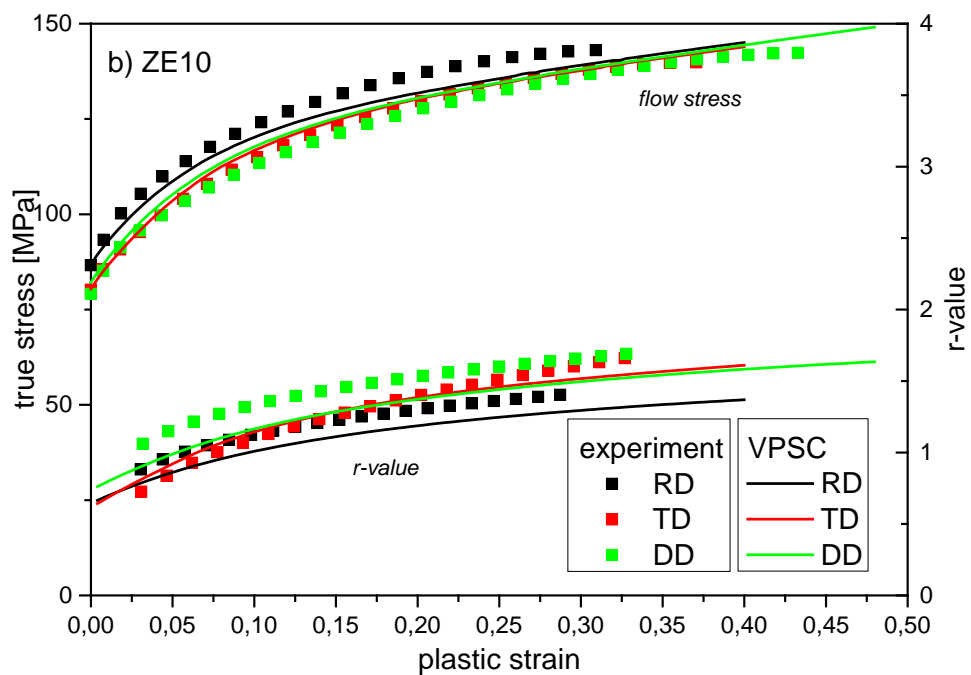


(b) ZE10

Figure 1 Basal (0002) and prismatic (10 $\bar{1}0$) pole figures of (a) AZ31 and (b) ZE10 in the as-received condition.



(a) AZ31



(b) ZE10

Figure 2 Flow stress and strain anisotropy evolution of (a) AZ31 and (b) ZE10 under uniaxial tension (RD, TD, and 45°) at 200°C, experiments and parameter fit.

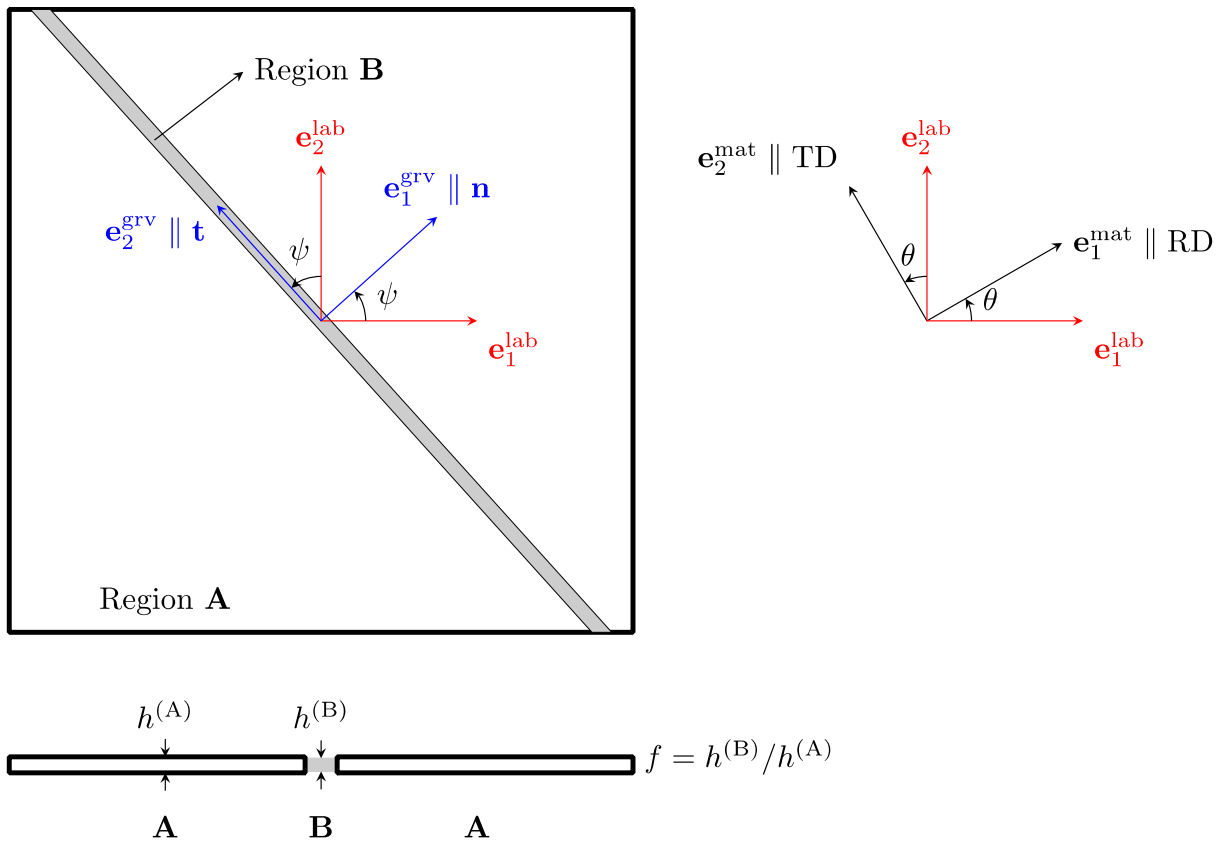


Figure 3 Schematic illustration of the Marciniak-Kuczyński model.

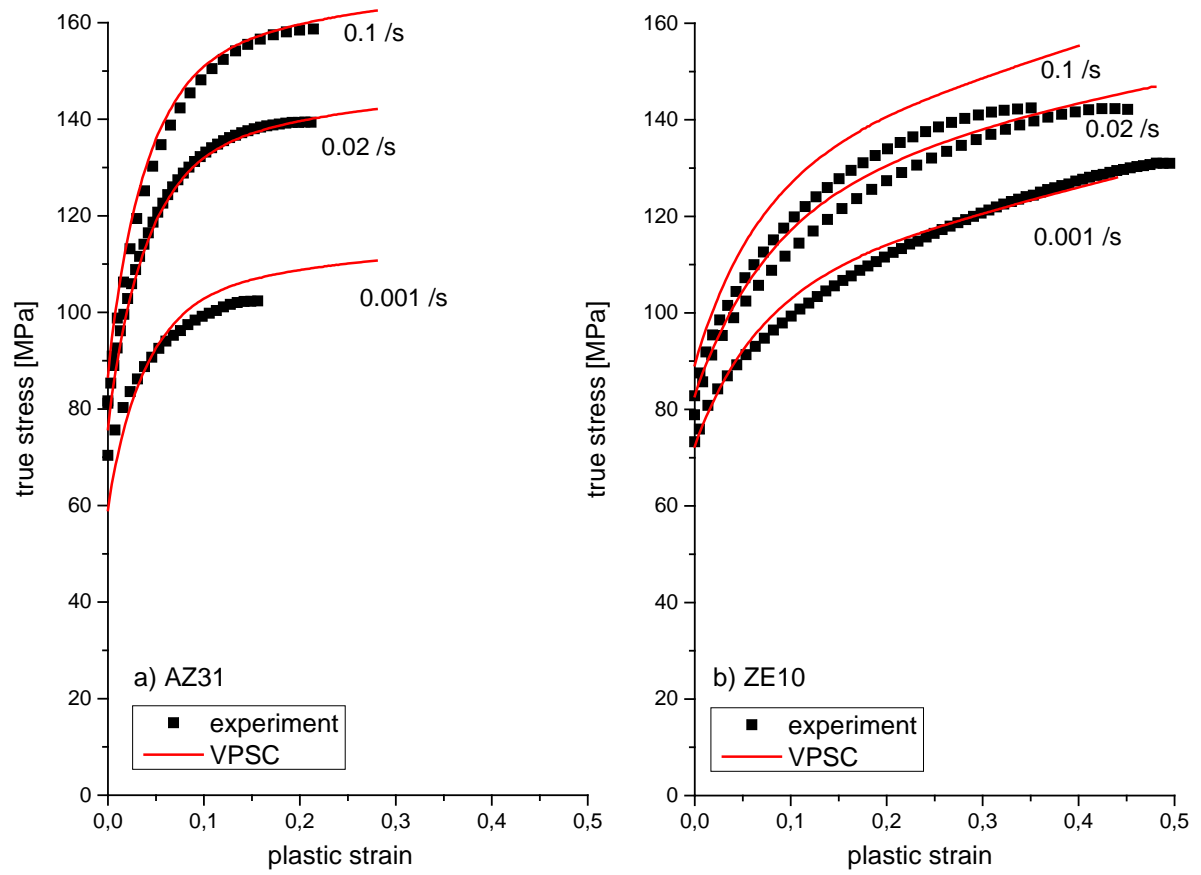
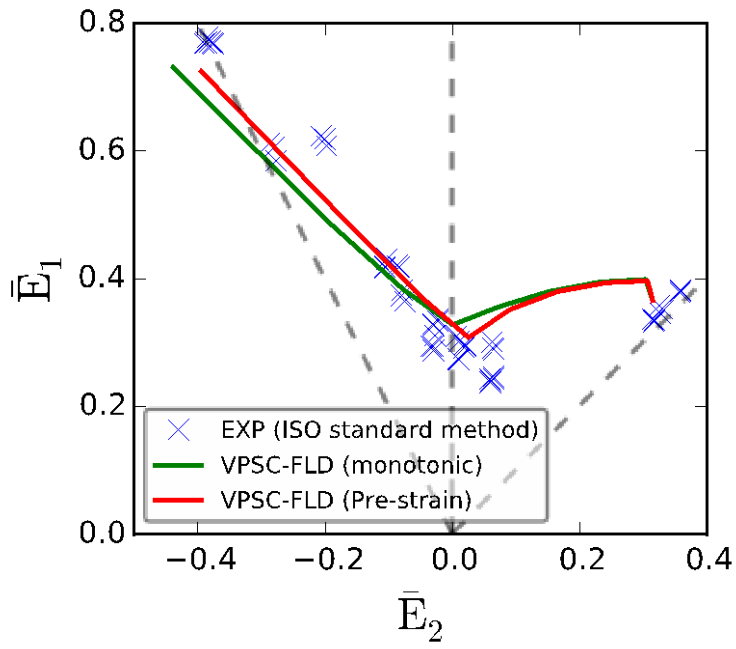
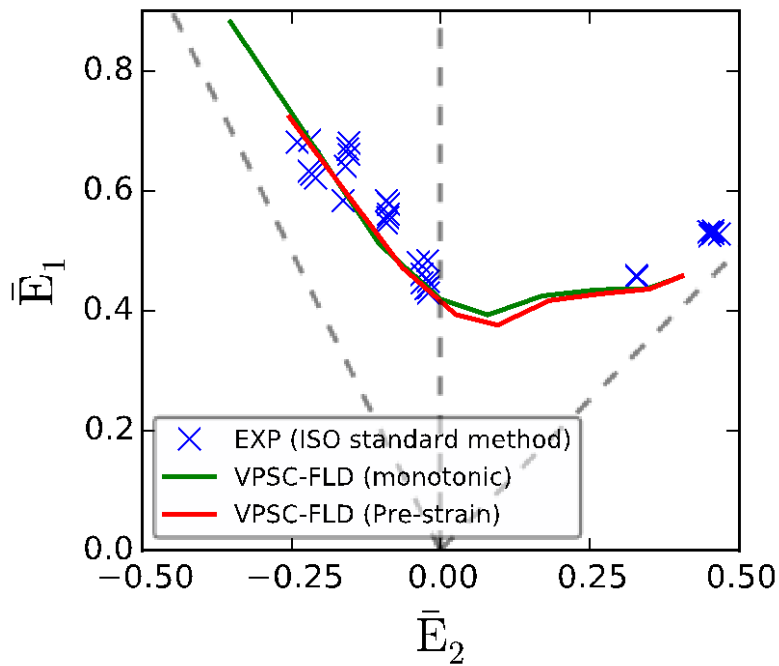


Figure 4 Rate-dependent stress-strain response of AZ31 and ZE10 evidenced during tensile testing along the RD (experiments and parameter fit).

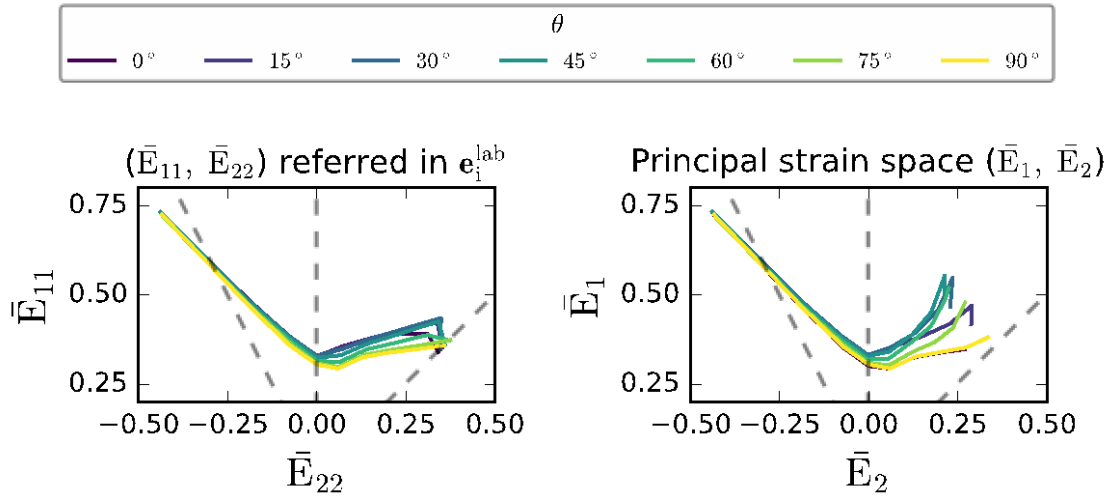


(a) AZ31



(b) ZE10

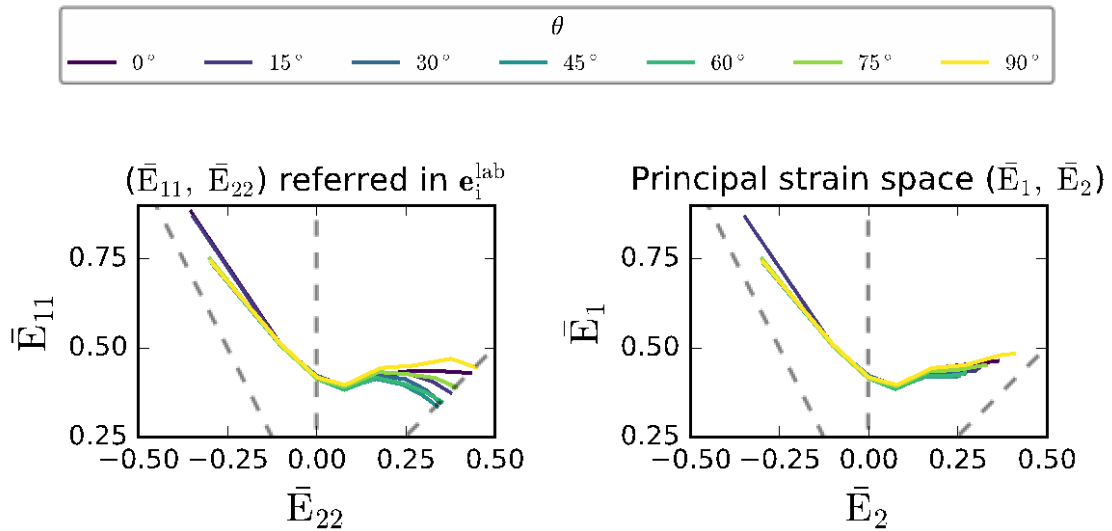
Figure 5 Experimental and predicted forming limits in the principal strain space for (a) AZ31 and (b) ZE10 with $\theta = 90^\circ$, both with and without biaxial pre-strain f_0 values of 0.995 and 0.999 for AZ31 and ZE10, respectively.



(a) FLCs plotted in $(\bar{E}_{11}, \bar{E}_{22})$ space

(b) FLCs plotted in the principal strain space

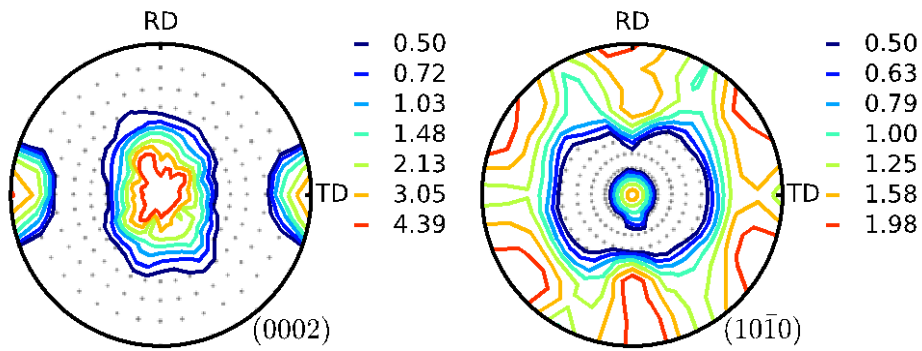
Figure 6 Predicted FLCs of AZ31 under various θ angles.



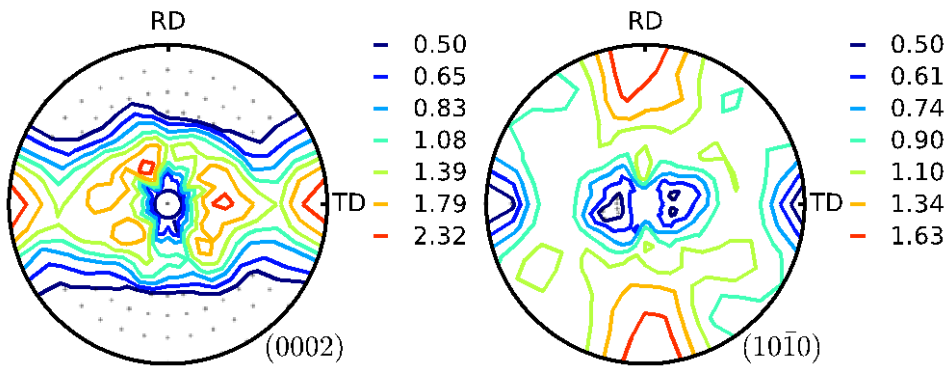
(a) FLCs plotted in $(\bar{E}_{11}, \bar{E}_{22})$ space

(b) FLCs plotted in the principal strain space

Figure 7 Predicted FLCs of ZE10 under various θ angles.



(a) AZ31



(b) ZE10

Figure 8 Initial $\{10\bar{1}2\}$ twinning induced textures resulting from pre-compression of 0.04 from (a) AZ31 and (b) ZE10.

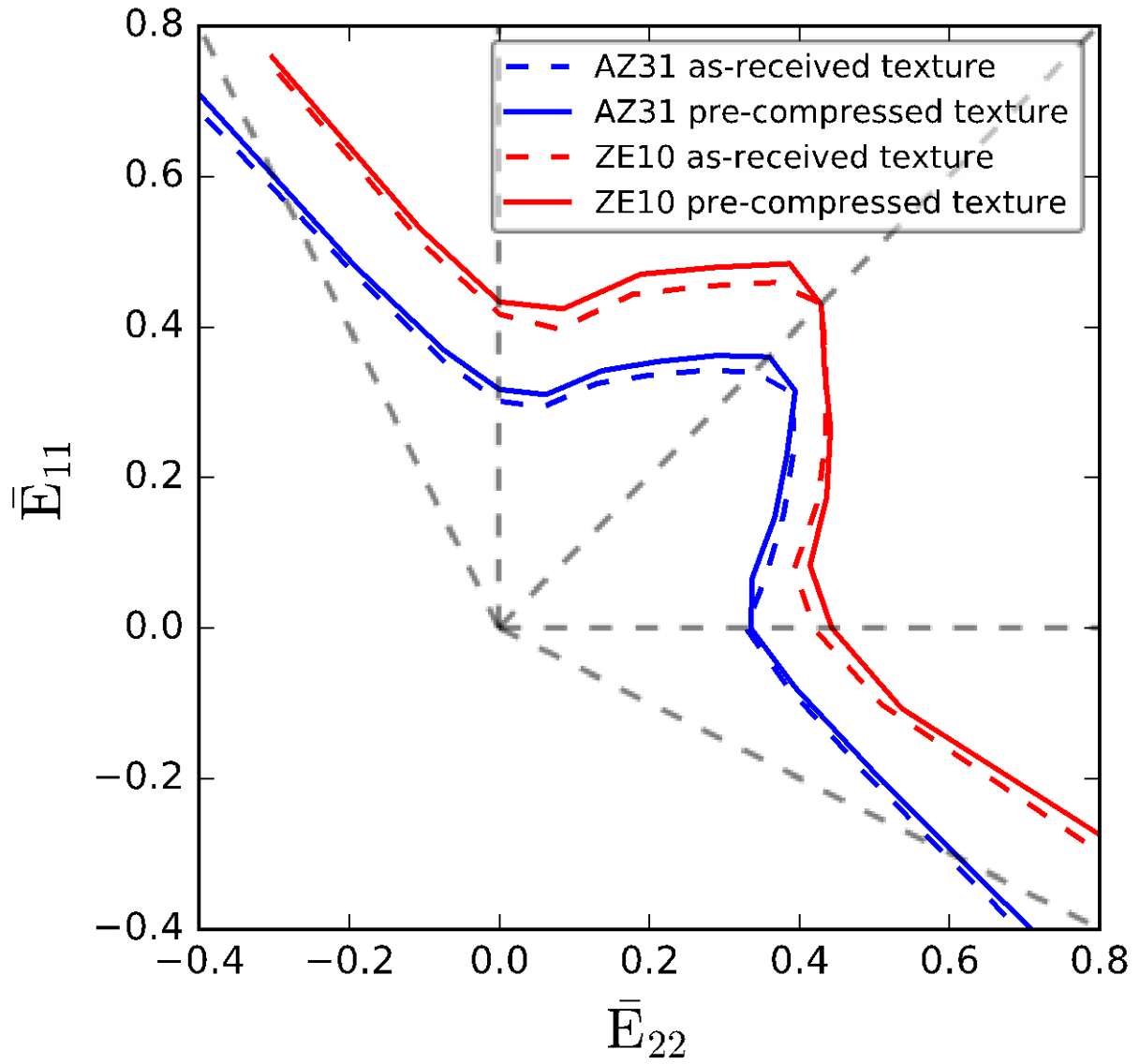
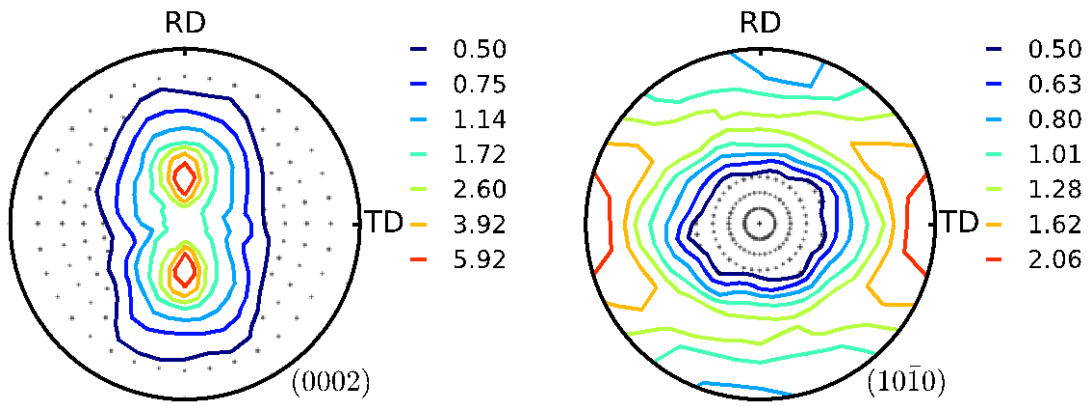
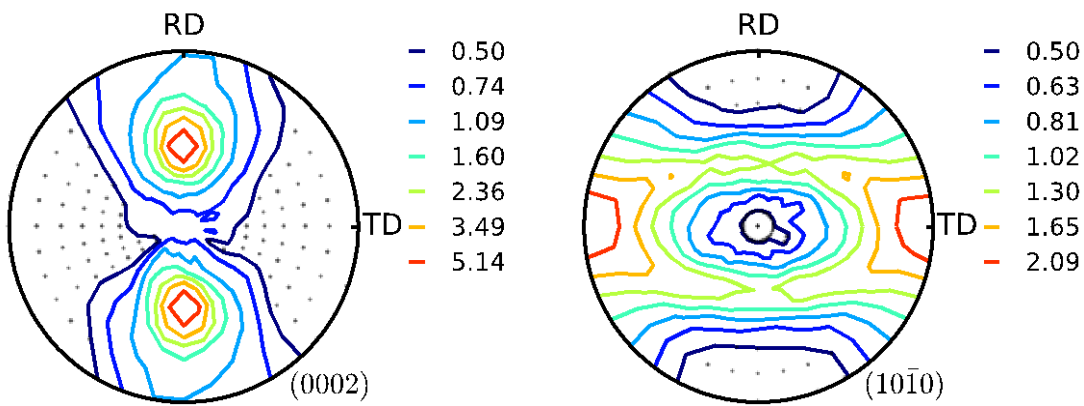


Figure 9 Comparison of the FLCs obtained from the as-received textures and those resulted from 0.04 pre-compression along the TD to induce $\{10\bar{1}2\}$ twin. For each case, the two FLCs ($\theta = 0^\circ$ and $\theta = 90^\circ$) are continuously combined to a single line in the $(\bar{E}_{11}, \bar{E}_{22})$ space.

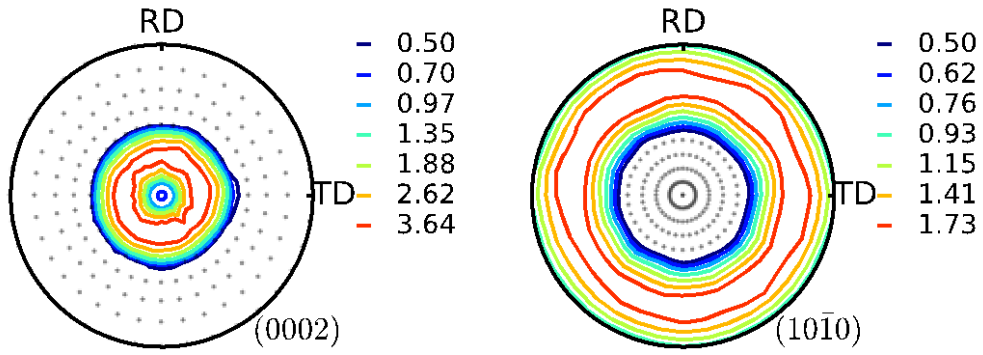


(a) 30° tilt (bipole30)

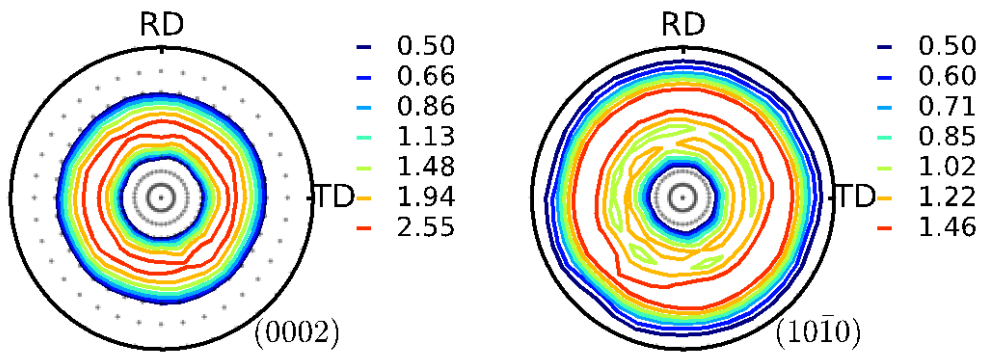


(b) 50° tilt (bipole50)

Figure 10 Model textures for AZ31. Doublets of basal poles tilted from the ND towards the RD by (a) 30° and (b) 50°.



(a) Basal fiber tilted from the ND by 30° (doughnut30)



(b) Basal fiber tilted from the ND by 50° (doughnut50)

Figure 11 Model textures for ZE10. Two doughnut-shaped basal pole fibers tilted symmetrically away from the ND by (a) 30° and (b) 50°.

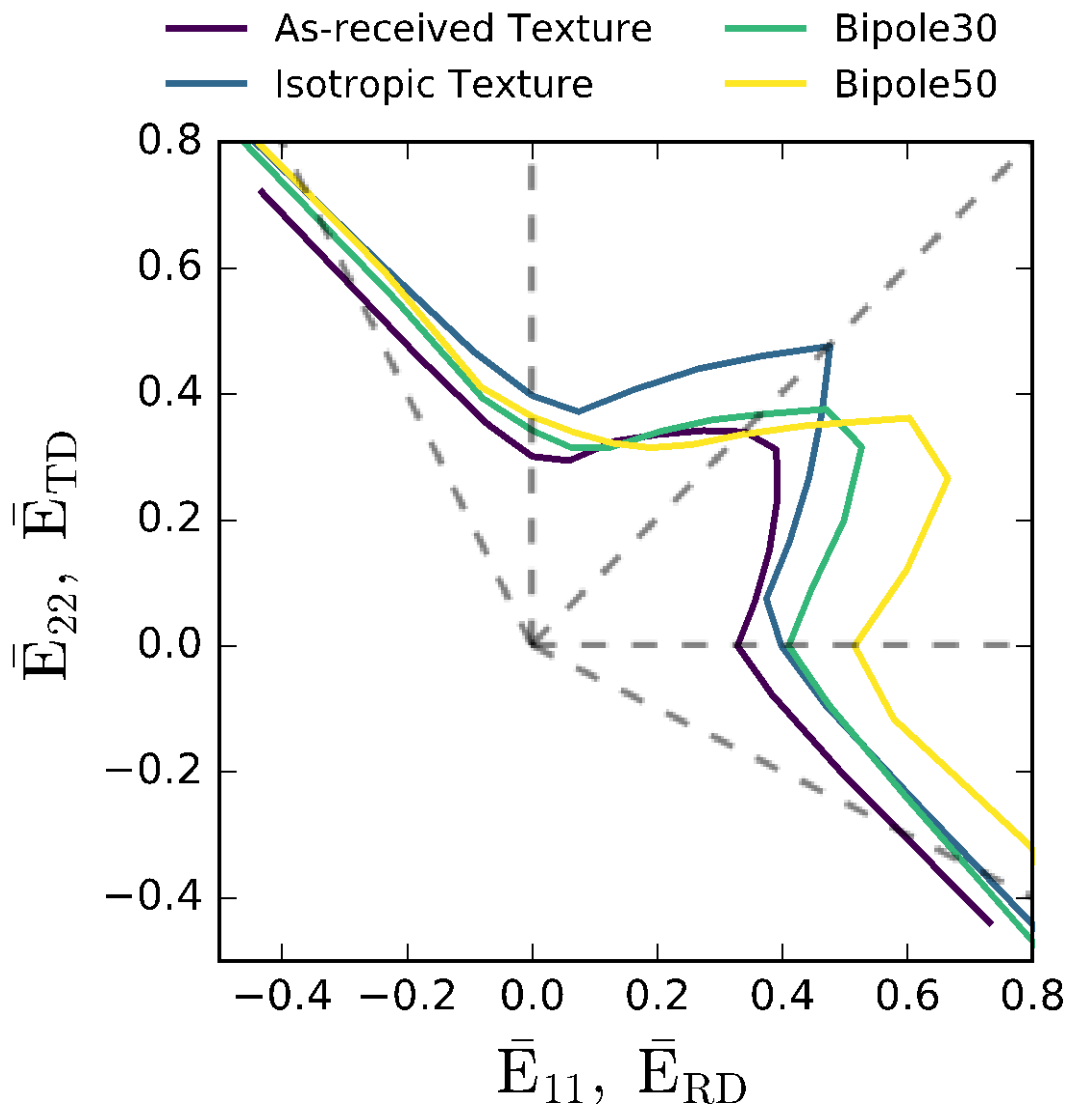


Figure 12 VPSC-FLD predictions using various textures for AZ31 ($\theta = 0^\circ$ and 90° with $f_0 = 0.995$).

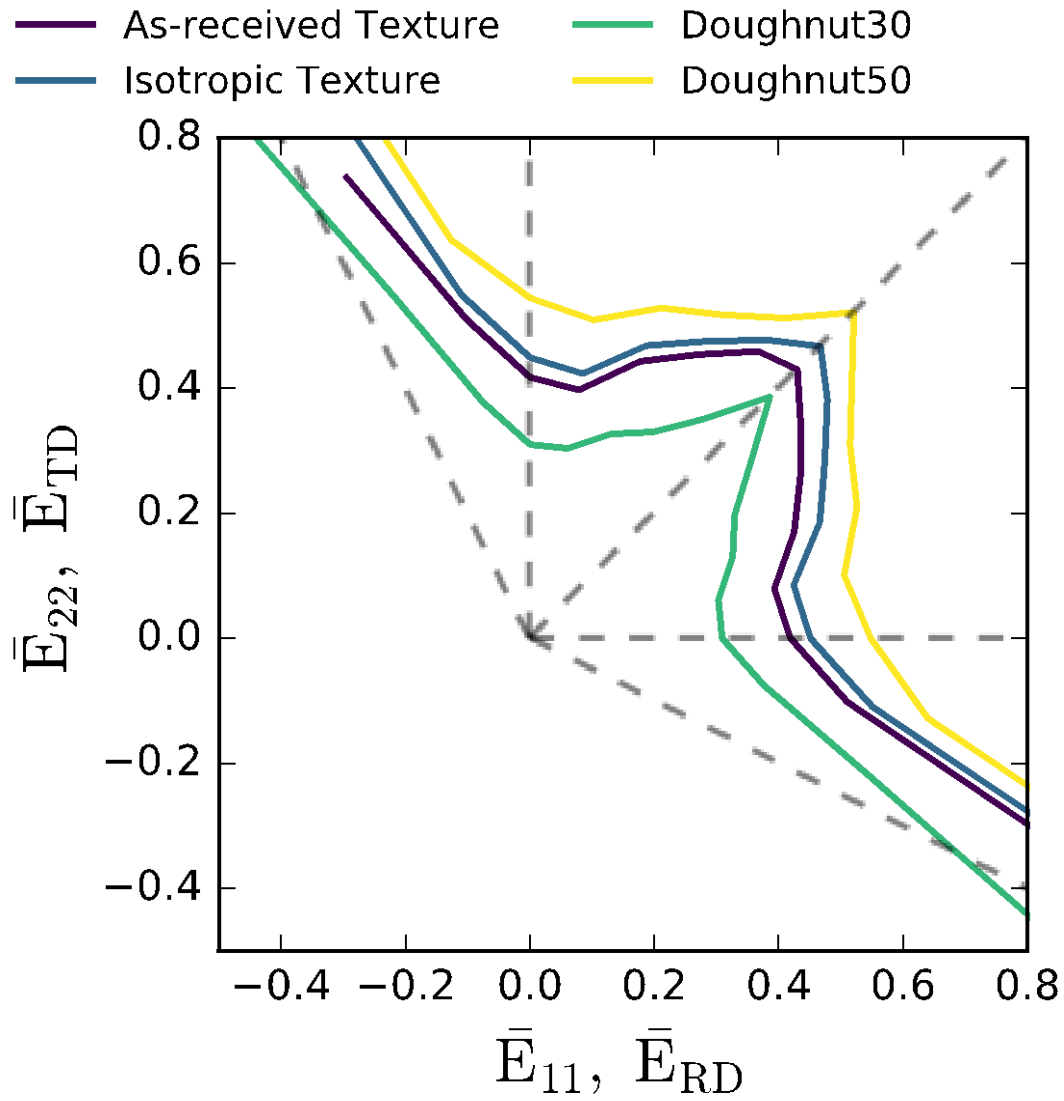


Figure 13 VPSC-FLD predictions using various textures for ZE10 ($\theta = 0^\circ$ and 90° with $f_0 = 0.999$).